aerospace

MDPI

Article

Optimizing Combustion Characteristics of Ammonium Perchlorate Composites with Nickel-Enhanced Carboxymethyl Cellulose

Marat Nurguzhin [1], Marat Janikeyev [1], Myrzakhan Omarbayev [1], Azira Yermakhanova [1], Mohammed Meiirbekov [1], Miras Zhumakhanov [1], Aidos Lesbayev [2], Darkhan Yerezhep [2], Meiram Atamanov [3], Marat Tulepov [4] and Zhansaya Beksultan [4,*]

[1] JSC "National Center for Space Research and Technology", Shevchenko Str., 15, Almaty 050010, Kazakhstan; nurguzhin.m@spaceres.kz (M.N.); m.janikeyev@spaceres.kz (M.J.); omarbayev.m@spaceres.kz (M.O.); a.yermakhanova@spaceres.kz (A.Y.); meiirbekov.m@spaceres.kz (M.M.); zhumakhan.miras@spaceres.kz (M.Z.)
[2] Intistute of Energy and Mechanical Engineering Named after A. Burkitbayev, Satbayev University, 22a Satpaev Str., Almaty 050013, Kazakhstan; a.lesbayev@satbayev.university (A.L.); darhan_13@physics.kz (D.Y.)
[3] Faculty of Natural Sciences, Kazakh National Women's Teacher Training University, Gogol Str., 114 k1, Almaty 050000, Kazakhstan; mk.atamanov@gmail.com
[4] Faculty of Chemistry and Chemical Technology, Al Farabi Kazakh National University, 71 al-Farabi Ave., Almaty 050040, Kazakhstan; tulepov@rambler.ru
* Correspondence: zhansayabeksultankyzy@mail.ru

Abstract: This study investigates the impact of nickel doping on the thermal and combustion properties of ammonium perchlorate/carboxymethyl cellulose (AP/CMC) composites. Through comprehensive SEM-EDS, FTIR, XRD, DSC, TGA, and burning rate analyses, significant improvements in the structural and functional characteristics of the AP/CMC-Ni composite were observed compared to those of pure AP and AP/CMC composites. The SEM-EDS analysis revealed that nickel incorporation resulted in thicker and more irregular CMC fibers, indicating substantial morphological changes. The FTIR spectroscopy showed shifts in the O-H and C=O stretching bands, pointing to interactions between nickel ions and CMC functional groups. The XRD patterns highlighted a decrease in crystallinity and the presence of NiO phases, confirming the successful integration of nickel into the CMC matrix. The thermal analysis demonstrated that nickel doping significantly lowered the decomposition temperature of the AP/CMC composite, as evidenced by DSC, and enhances the thermal degradation process, as shown by TGA. The AP/CMC-Ni composite exhibited a higher burning rate across all of the tested pressures, highlighting the catalytic effect of nickel in improving the combustion efficiency. The burning rate for AP/CMC follows the power-law expression with constants a = 2.34 and n = 0.499, while for AP/CMC-Ni, the constants are a = 3.35 and n = 0.475. This study highlights the essential role of nickel doping in facilitating the decomposition of AP within the AP/CMC composite. By lowering the decomposition temperature, nickel enhances the overall combustion process, making the AP/CMC-Ni composite more efficient for applications requiring controlled thermal decomposition. These findings provide valuable insights for the design and development of high-performance composite materials in advanced industrial applications.

Keywords: nickel doping; ammonium perchlorate; carboxymethyl cellulose; thermal decomposition; combustion efficiency

check for updates

Academic Editor: Kyun Ho Lee

Received: 19 February 2025
Revised: 21 March 2025
Accepted: 21 March 2025
Published: 23 March 2025

Citation: Nurguzhin, M.; Janikeyev, M.; Omarbayev, M.; Yermakhanova, A.; Meiirbekov, M.; Zhumakhanov, M.; Lesbayev, A.; Yerezhep, D.; Atamanov, M.; Tulepov, M.; et al. Optimizing Combustion Characteristics of Ammonium Perchlorate Composites with Nickel-Enhanced Carboxymethyl Cellulose. *Aerospace* **2025**, *12*, 270. https://doi.org/10.3390/aerospace12040270

Copyright: © 2025 by the authors. Licensee MDPI, Basel, Switzerland. This article is an open access article distributed under the terms and conditions of the Creative Commons Attribution (CC BY) license (https://creativecommons.org/licenses/by/4.0/).

1. Introduction

The development of advanced composite materials with enhanced thermal and combustion properties is of paramount importance in various industrial applications, partic-

ularly in the fields of aerospace, rocket fuels, pyrotechnics, and energy storage systems. Ammonium perchlorate (AP) is widely used as an oxidizer in solid rocket propellants due to its high oxygen content and favorable thermal decomposition characteristics [1–4]. It is well known that the inclusion of additional components in AP-based composites is crucial for improving their overall combustion characteristics and efficiency [5–7].

Carboxymethyl cellulose (CMC) is a water-soluble polymer derived from cellulose, is known for its excellent film-forming properties, high viscosity, biodegradability, and affordable cost [8]. It is commonly used as a binder and stabilizer in various composite materials, enhancing their mechanical and thermal properties [9,10]. In addition to these advantages, CMC can be further improved by incorporating catalytic elements into its structure [11–13]. Doping CMC with catalysts can significantly alter its physical and chemical properties, leading to higher efficiency in numerous applications [14–16]. Catalysts such as transition metals have the potential to accelerate decomposition processes, thereby increasing the rate of combustion and overall energy release [17,18]. The introduction of catalytic elements into CMC can facilitate the faster and more complete oxidation of fuel components [19,20]. For example, studies have shown that catalysts such as Fe_2O_3, CuO, NiO, and metal nanoparticles supported on graphene oxide enhance the thermal decomposition of oxidizers like AP, resulting in improved combustion performance [21–23]. These catalysts promote the breakdown of the oxidizer at lower temperatures, thereby increasing the combustion efficiency and delivering more consistent and controlled energy release.

Among these catalysts, nickel has been identified as being particularly effective for enhancing the thermal decomposition of AP [24,25]. For instance, research indicates that nickel nanoparticles, when combined with materials such as graphene, can decrease the decomposition temperature of AP by up to 122 °C, thereby significantly improving its thermal decomposition efficiency [26]. Another study highlighted that nickel-doped catalysts not only accelerate the decomposition rate of AP but also improve the overall combustion process, making the propellant burn more efficiently and reliably [27]. These findings, supported by various investigations into the catalytic effects of nickel and its compounds on AP [28–30], suggest that integrating nickel into CMC-based composites could facilitate faster and more efficient thermal decomposition of the oxidizer.

This study aims to investigate the effects of nickel doping on the thermal and combustion behavior of AP/CMC composites. By employing a combination of analytical techniques—including SEM-EDS, FTIR, XRD, DSC, TGA, and burning analysis—we seek to comprehensively understand the structural changes and performance enhancements induced by nickel incorporation. The findings of this research will provide valuable insights into the design and development of high-performance composite materials for advanced industrial applications.

2. Experimental Procedures

The schematic illustrated in Figure 1 details the fabrication process of AP/CMC-Ni composites. Initially, nickel nitrate hexahydrate $Ni(NO_3)_2 \cdot 6H_2O$ in various concentrations ranging from 1 to 4 M solutions is blended with CMC powder. This blend is then sonicated at frequencies ranging from 20 to 60 kHz and an energy flux density on the order of 0.1 W/cm^2 for 20 min, at temperatures between 2 and 5 °C. This process ensures thorough integration of nickel ions into the CMC, forming the CMC-Ni complex. After sonication, the CMC–Ni blend was vacuum-filtered by transferring it to a Büchner funnel and applying reduced pressure using a laboratory vacuum pump. This step effectively removes unreacted nickel ions and by-products, yielding a purified CMC–Ni complex before subsequent drying by heating at 70 °C for 2 h. The dried material was then ground into a uniform mass using a conventional hammer mill (Altimax GR-1-1500, Alta, China).

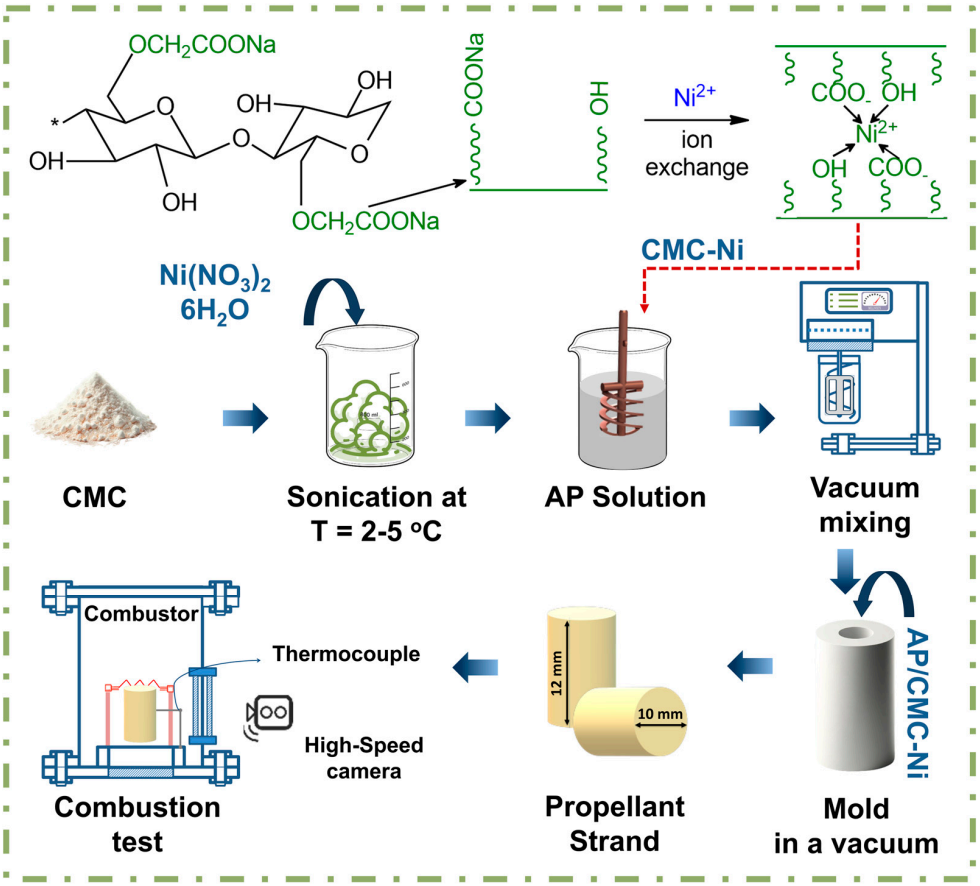

Figure 1. Schematic representation of the AP/CMC-Ni composite fabrication.

Following this, the complex (either CMC or CMC-Ni) is added to a solution consisting of AP (Figure S1) dissolved in acetone, where acetone comprises 3% of the total mass, with the AP to complex ratio set at 7:3. Notably, the 7:3 ratio of AP to the complex was investigated due to its potential for optimizing combustion properties, as formulations with AP at complex ratios of 8:2 and 6:4 demonstrated lower burning rates compared to this mixture.

To remove any air bubbles and ensure a dense, uniform composite, the mixture undergoes vacuum mixing. The vacuum-treated mixture is subsequently molded under vacuum conditions to shape it into propellant strands with specific geometries. Finally, these strands undergo combustion testing in a controlled setup where ignition wires and thermal couples ignite the sample, and a high-speed camera records the combustion characteristics. This test evaluates the burn rate, stability, and energetic properties of the propellant, crucial for its potential applications, such as in rocket propulsion. Subsequently, the mixture was poured into a Teflon mold to form a sample with a height of 11 mm, a diameter of 10 mm, and a mass of around 1 g. The sample was equipped with a K-type thermocouple and a heating coil to initiate the combustion of the sample.

The linear burning rates of AP/CMC and AP/CMC-Ni samples were measured at various pressures. The burning rate for both samples increases with pressure, indicating a pressure-dependent combustion behavior. This relationship follows the following power-law expression:

$$r = a \cdot P^n \quad (1)$$

where r represents the burning rate and P is the pressure [31]. This equation is fundamental in the study of propellants, as it describes how the burning rate varies with pressure, a key factor in understanding combustion characteristics under different conditions.

To capture the temperature evolution during combustion, each sample was equipped with a thermocouple. The temperature data were recorded in real time using a digital data acquisition system (Potentiostat-Galvanostat P-40X, Electrochemical Instruments, Russia). From these measurements, the derivative of the temperature profile (dT/dt) was calculated to assess the rate of heat release. The maximum temperature (T_{max}) and the time to reach T_{max} were then determined for each sample under the same ignition conditions, enabling direct comparisons between AP/CMC and AP/CMC–Ni formulations.

Each experimental measurement including SEM-EDS, DSC-TG, and burning rate tests was performed in triplicate to ensure repeatability. We also conducted a supplementary elemental analysis on selected samples using different instrumentations to verify consistency and minimize potential errors, with full details provided in the Supporting Information file.

3. Results

In Figure 2, SEM and EDAX mapping analyses of the investigated samples are presented, comparing pure CMC (Figure 2a) with nickel-doped CMC (CMC-Ni) (Figure 2b). The SEM images reveal distinct structural differences: Pure CMC (Figure 2a) consists of elongated, smooth fibrous structures, characteristic of its natural morphology. This commercial CMC typically contains sodium, which facilitates the initial interaction with nickel due to the presence of carboxymethyl chains attached to the CMC's pyranose ring [32].

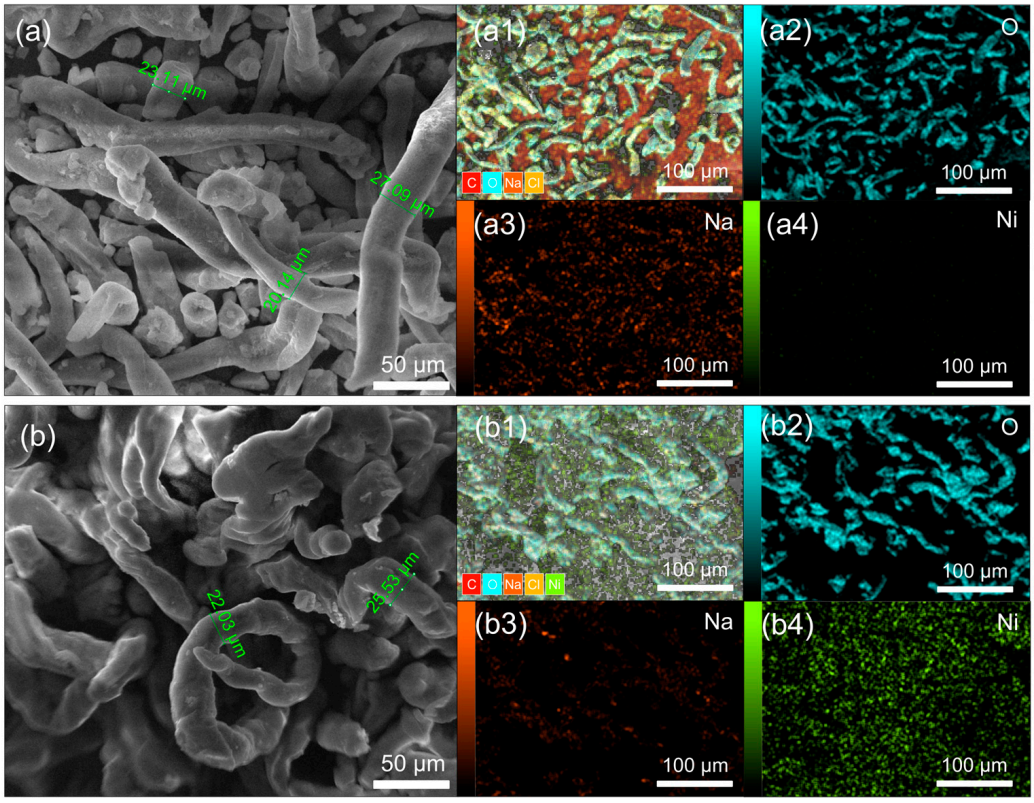

Figure 2. Comparative SEM images and EDAX mappings of (**a**) pure CMC and (**b**) nickel-doped CMC (CMC-Ni). SEM images and EDAX mapping of the distribution of main elements (**a1**,**b1**)–C, O, Na, Cl, Ni; (**a2**,**b2**)-O; (**a3**,**b3**)-Na; (**a4**,**b4**)-Ni.

In contrast, CMC-Ni (Figure 2b) exhibits fibers that have partially fused together, losing their smooth structure. Additionally, the fibers appear to expand and contract irregularly along their length, likely due to the influence of water and nickel salt during the modification process. This suggests that nickel incorporation induces structural rearrangements, affecting the material's microstructure.

The EDAX mapping in Figure 2 illustrates the elemental distribution in the samples, confirming the presence of sodium in pure CMC and the introduction of nickel in the CMC-Ni sample. The EDAX spectra in Figure 3 and additional EDAX spectra and mass ratio data are provided in Figures S2 and S3 (Supplementary File). The detailed quantitative analysis showed a decrease in the sodium content from 11.46 Wt% in the pure CMC to 2.29 Wt% in the CMC-Ni, while nickel reached 21.76 Wt% in the modified sample. These data indicate an ionic exchange between Ni^{2+} and Na^{+} within the material structure.

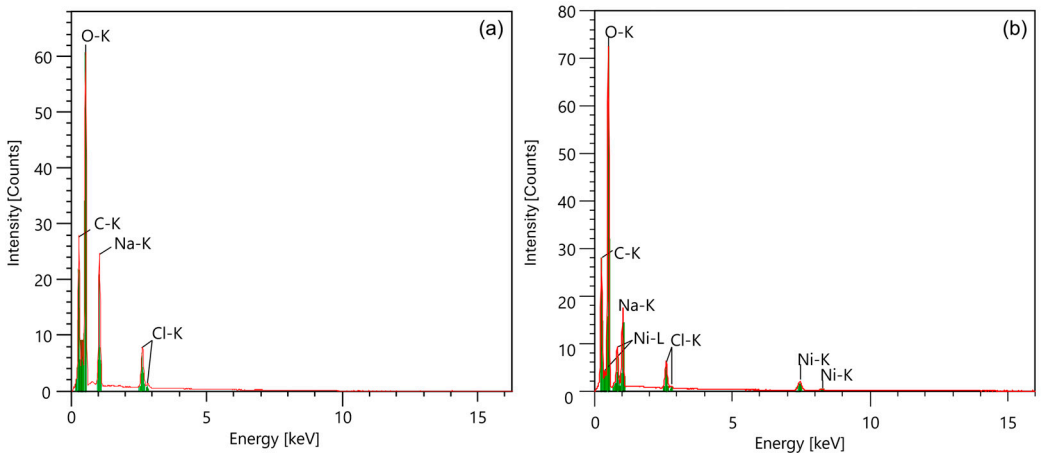

Figure 3. The EDAX spectra of CMC (**a**) and CMC-Ni (**b**).

Figure 4 presents the particle size distribution for pure CMC (Figure 4a) and nickel-doped CMC (CMC-Ni, Figure 4b). The histograms illustrate the frequency of particle sizes within each sample, providing insight into how nickel incorporation affects the material's microstructure.

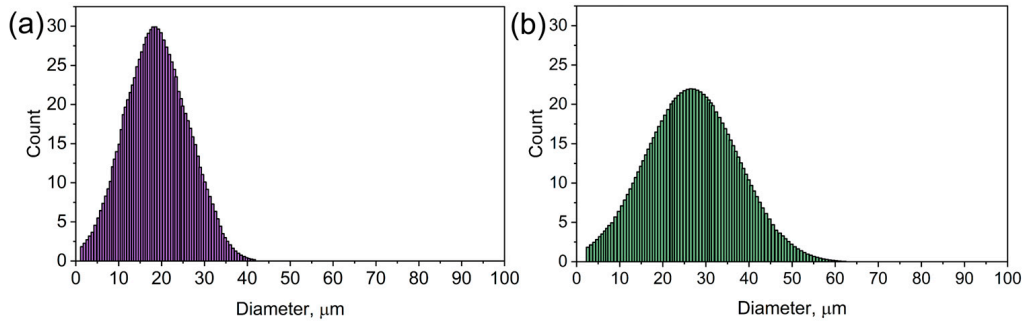

Figure 4. The particle size distribution of CMC (**a**) and CMC-Ni (**b**).

In Figure 4a (pure CMC), the particle size distribution is narrower and more symmetric, with the highest frequency occurring around 20–25 μm. This indicates a relatively uniform structure with a well-defined particle size. In Figure 4b (CMC-Ni), the distribution shifts toward larger particle sizes, with the peak around 30 μm and a broader range extending beyond 50 μm. This suggests that nickel doping leads to particle agglomeration and growth, likely due to the interaction of nickel salts with the CMC matrix during synthesis. The expansion and contraction along the fiber structure observed in the SEM images further support this structural transformation.

Figure 5a shows the Fourier transform infrared (FTIR) spectroscopy results comparing the spectral profiles of pure CMC and CMC-Ni. The FTIR spectrum of pure CMC shows prominent absorption peaks at 3435 cm^{-1}, attributed to the O–H valence vibration, and at 2925 cm^{-1}, associated with the C–H valence vibration. Other significant peaks include

the carbonyl (C=O) group at 1628 cm^{-1} and the carboxylate (COO-) group at 1426 cm^{-1}, indicating the presence of these functional groups in the CMC structure [33].

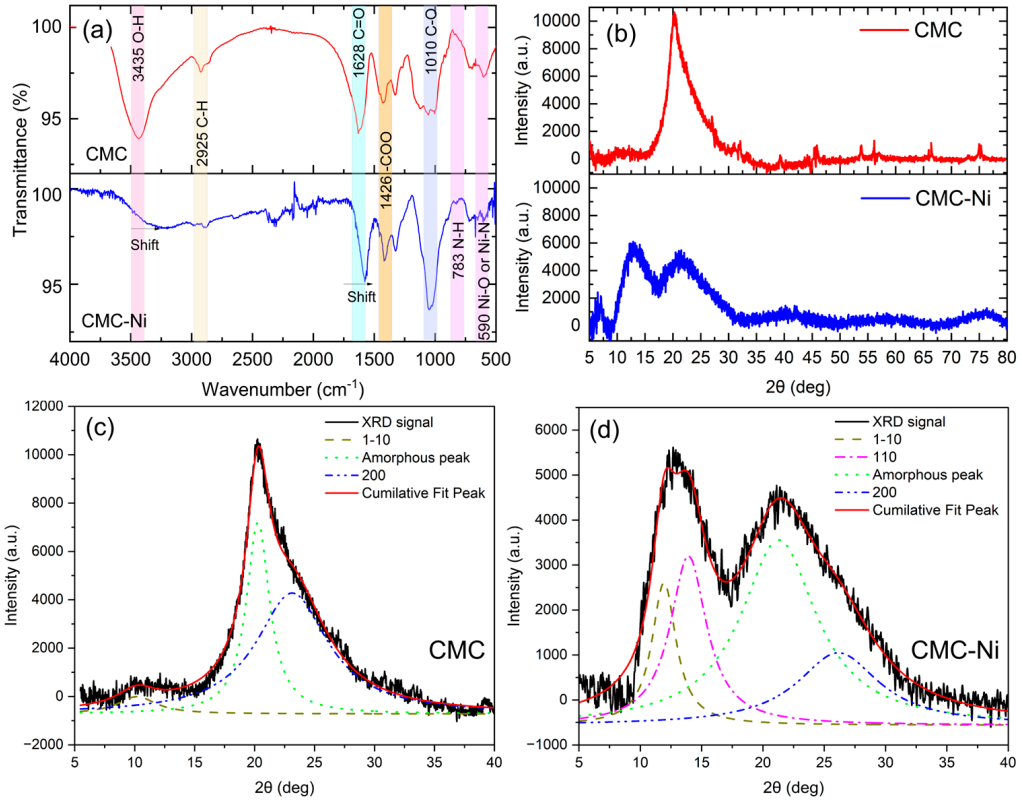

Figure 5. Characterization of carboxymethyl cellulose (CMC) and nickel-doped CMC (CMC-Ni): (**a**) FTIR spectra; (**b**) XRD patterns; (**c**) deconvolution of XRD peaks for pure CMC; (**d**) deconvolution of XRD peaks for CMC–Ni.

The spectrum of CMC-Ni in Figure 5a shows prominent shifts and decreases in transmittance in these absorption bands. It was found that the O-H peak at 3435 cm^{-1} and the C=O peak at 1628 cm^{-1} both shifted, suggesting interactions between nickel ions and these functional groups. This interaction probably alters the hydrogen bonding network within the CMC matrix and may affect the coordination environment of nickel ions [34]. The shifts in these peaks indicate chemical modifications of the polymer structure due to the incorporation of nickel, affecting its overall properties and potential applications [35]. Moreover, there were slight changes in the intensities of the peaks at 783 and 590 cm^{-1} after the incorporation of Ni, which could be due to the formation of N single bond Ni and O single bond Ni [36,37].

The FTIR spectra for 1 M, 2 M, 3 M, and 4 M Ni concentrations (provided in Figure S4) revealed that higher Ni concentrations (≥3 M) led to significant structural distortions, while 1 M showed weaker Ni-CMC interactions. Based on this analysis, 2 M was selected as the optimal concentration, ensuring effective Ni incorporation while maintaining structural integrity.

In Figure 5b, the XRD patterns of CMC and CMC-Ni are shown over the 5–80° (2θ) range. To achieve the precise separation of crystalline and amorphous contributions, curve-fitting techniques using Lorentzian and Gaussian (Figure S5) functions were employed [38–40]. The detailed methodology and calculation procedure are provided in the Supporting Information (SI) file. The CMC sample exhibits a peak at ~20–22° (2θ), corresponding to the amorphous phase with an underlying crystalline (200) reflection [41]. In contrast, CMC-Ni displays a broader peak with reduced intensity, suggesting decreased

crystallinity due to nickel incorporation. Additional peaks at ~10–15° (2θ) indicate possible Ni-related structural modifications within the CMC matrix.

To better distinguish the crystalline and amorphous phases, peak deconvolution was applied. The deconvoluted XRD pattern for CMC (Figure 5c) reveals the hidden (200) crystalline reflection, characteristic of cellulose, beneath the dominant amorphous peak at ~20–22° (2θ). Additionally, the (1–10) peak at ~12–14° (2θ) is present, indicating structured but partially disordered regions.

In CMC-Ni (Figure 5d), significant structural changes are observed. The amorphous contribution increases, and the (200) crystalline peak is further obscured, confirming a loss of crystallinity upon nickel incorporation. A distinct (110) peak at ~15° (2θ), absent in pure CMC, appears in CMC-Ni, suggesting that nickel interacts with the cellulose matrix, leading to a rearrangement of structural domains. This interaction likely promotes Ni-coordinated modifications, stabilizing specific regions while increasing overall disorder.

The crystallinity index, calculated from the deconvoluted peaks, decreases from 48.7% in CMC to 26.6% in CMC-Ni, confirming that nickel incorporation disrupts the ordered cellulose structure and enhances the amorphous phase. These structural changes indicate a fundamental alteration in the crystallization behavior of CMC due to nickel integration.

These results collectively suggest that nickel ions interact with the oxygen-bearing functional groups of CMC, reducing the cellulose's crystalline order and expanding amorphous domains. Such disruption can enhance the mobility of polymer chains and improve the diffusion pathways for heat and reactive species, factors known to accelerate combustion reactions. Consequently, Ni doping not only modifies the hydrogen bonding network but also promotes more efficient energy release during thermal decomposition. This synergistic effect between nickel-incorporated CMC and AP aligns with the improved combustion performance observed in the provided results.

Figure 6 presents the differential scanning calorimetry (DSC) and thermogravimetric analysis (TGA) results for pure AP (Figure 6a), pure CMC (Figure 6b), AP/CMC (Figure 6c), and AP/CMC-Ni (Figure 6d) composites. Figure 6a shows that the pure AP exhibits two distinct exothermic peaks corresponding to its thermal decomposition stages: low-temperature decomposition (LTD) at 301 °C and high-temperature decomposition (HTD) at 376 °C, where AP undergoes partial decomposition, releasing intermediate gaseous products such as HCl, Cl_2, and O_2 [42,43]. The TG curve for pure AP shows a mass loss of 96.9% upon heating, which corresponds to its decomposition.

The AP/CMC (Figure 6c) composite displays two distinct endothermic peaks at 346 °C and 417 °C, suggesting a complex decomposition process influenced by the presence of CMC. For the AP/CMC composite, the mass loss decreases to 92.2%, reflecting the additional decomposition of CMC.

In the AP/CMC-Ni composite (Figure 6d), a significant shift in the decomposition temperature is observed, with an endothermic peak appearing at 274 °C. This notable reduction in the decomposition temperature indicates a catalytic effect of nickel on the thermal degradation of the composite, enhancing the decomposition process. The AP/CMC-Ni composite shows an even higher mass loss of 99.1%, indicating nearly complete decomposition. The presence of nickel appears to facilitate the thermal degradation of the composite, likely due to its catalytic properties, which promote the breakdown of both AP and CMC components.

These thermal analysis results show that nickel doping significantly modifies the AP/CMC composite's thermal behavior, lowering the decomposition temperature and increasing the mass loss. This synergy may be attributed to localized catalytic sites formed when reactive intermediates from AP's initial decomposition interact with nickel, accelerating the breakdown of the CMC matrix. By lowering the overall activation energy, Ni doping ensures a more thorough conversion of both fuel and binder into gaseous products,

leading to an improved decomposition profile. Consequently, Ni-doped composites appear advantageous for applications requiring efficient and rapid thermal decomposition.

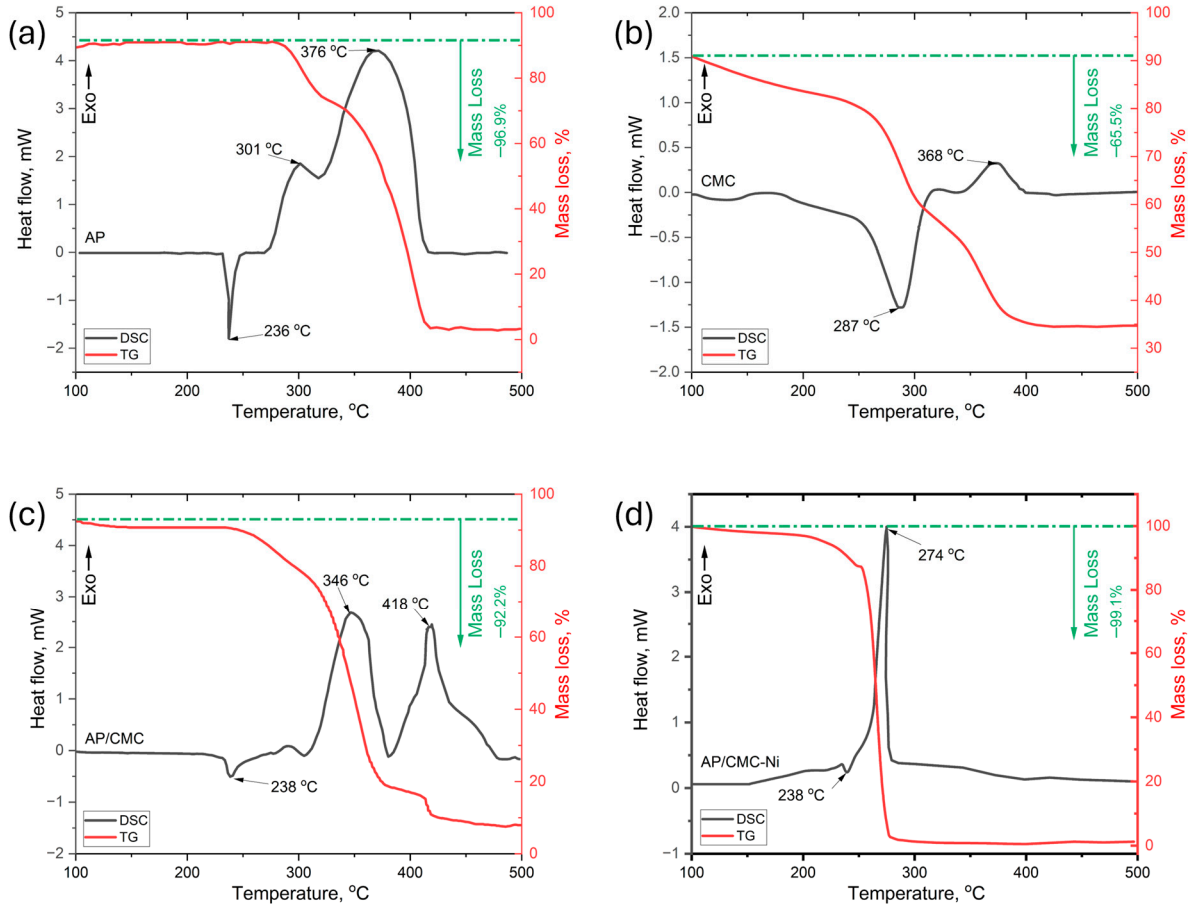

Figure 6. DSC and TG curves for pure AP (**a**), pure CMC (**b**), AP/CMC (**c**), and AP/CMC-Ni (**d**).

Figure 7 presents a frame-by-frame sequence of the combustion process for AP/CMC and AP/CMC–Ni samples at a 70:30 ratio under atmospheric conditions. Figure 7a illustrates the combustion of the AP/CMC sample. Ignition begins at 0 s, followed by the progression of the combustion front from 4 s to 21 s. The combustion front advances steadily overall, with the flame propagating through the sample. Although the flame height and intensity generally increase over time, occasional fluctuations indicate that the combustion is somewhat less stable compared to the Ni-doped composite (Figure 7b).

Figure 7b depicts the combustion of the AP/CMC-Ni sample. Ignition occurs at 0 s, with subsequent frames captured at 4–14 s. Compared to AP/CMC, the AP/CMC-Ni sample burns faster and more intensely. The flame propagates quickly, reaching its peak height and intensity earlier, indicating an enhanced combustion process due to nickel incorporation. Although the flame front appears steady from ignition, nickel incorporation accelerates the overall decomposition process, causing the system to reach its maximum flame height and intensity earlier than the pure AP/CMC sample. Consequently, the sample can maintain a visually steady burn while simultaneously achieving its peak combustion state at an earlier time. The frame-by-frame analysis of the combustion process demonstrates that nickel doping significantly influences the combustion behavior of the AP/CMC composite. The AP/CMC-Ni sample exhibits faster and more vigorous combustion compared to the AP/CMC sample. This enhanced combustion performance can be attributed to the catalytic effect of nickel, which facilitates the thermal degradation and combustion of the composite material. The rapid propagation of the combustion front and

the increased flame intensity suggest that nickel doping improves the overall combustion efficiency of the composite.

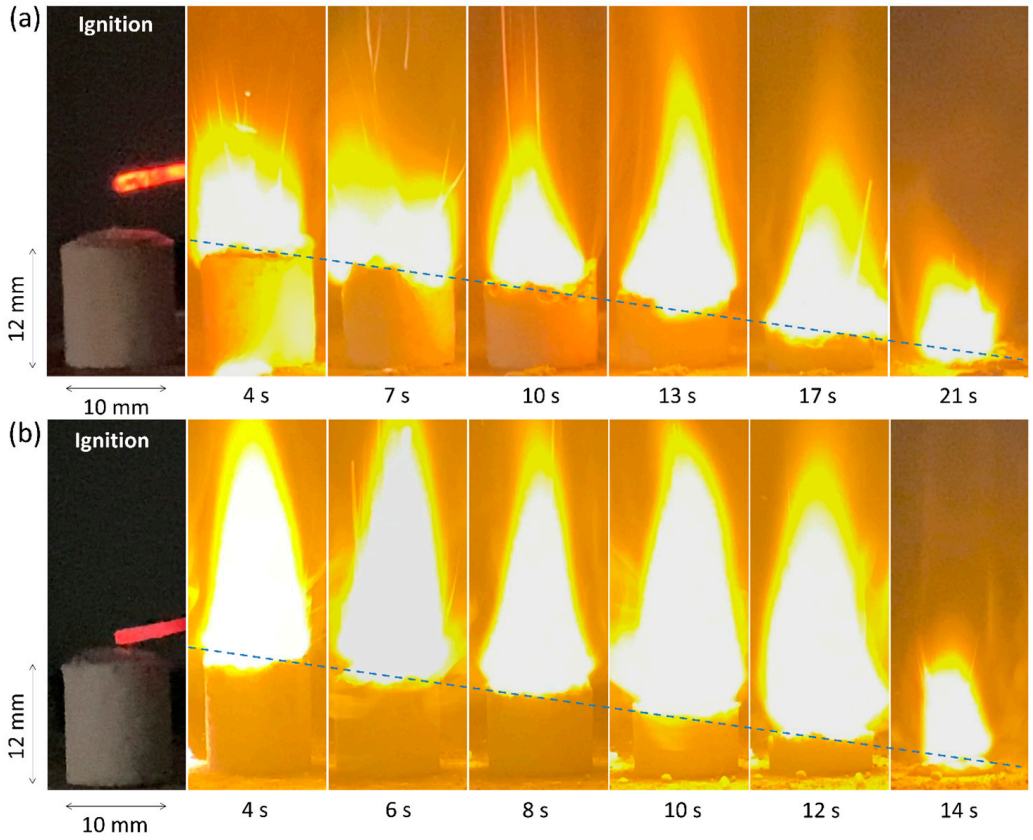

Figure 7. Frame-by-frame images of combustion of (**a**) AP/CMC and (**b**) AP/CMC-Ni samples at a ratio of 70/30 at atmospheric pressure.

The pressure exponent values show that while both composites are pressure-dependent, the AP/CMC-Ni sample is slightly less sensitive to pressure changes (0.499 vs. 0.475). The higher a value for the AP/CMC-Ni sample suggests that nickel doping increases the overall burning rate of the composite. Understanding the burning rate as a function of pressure is crucial for designing propellant grains and predicting rocket motor performance. The enhanced burning rate of AP/CMC-Ni indicates its potential for applications requiring higher combustion efficiency.

Figure 8b presents the thermal profile of the AP/CMC sample, illustrating the temperature evolution during combustion. The blue curve represents the temperature profile, while the red curve (*dT/dt*) corresponds to the rate of temperature change. The maximum temperature (T_{max}) reached during combustion is 1105 °C, with a time to T_{max} of 5.21 s. The gradual increase in temperature and the lower *dT/dt* values indicate a relatively slower combustion process, suggesting that the decomposition and energy release are more distributed over time.

Figure 8 presents the linear burning rates at different pressures from 0.1 to 1 MPa and the thermal profiles of the AP/CMC and AP/CMC-Ni samples. Figure 8a shows that AP/CMC-Ni burns faster than AP/CMC at all of the tested pressures under nitrogen pressure. The burning rate follows a power-law expression, with a = 2.34, n = 0.499 for AP/CMC and a = 3.35, n = 0.475 for AP/CMC-Ni, indicating that nickel doping enhances the combustion efficiency.

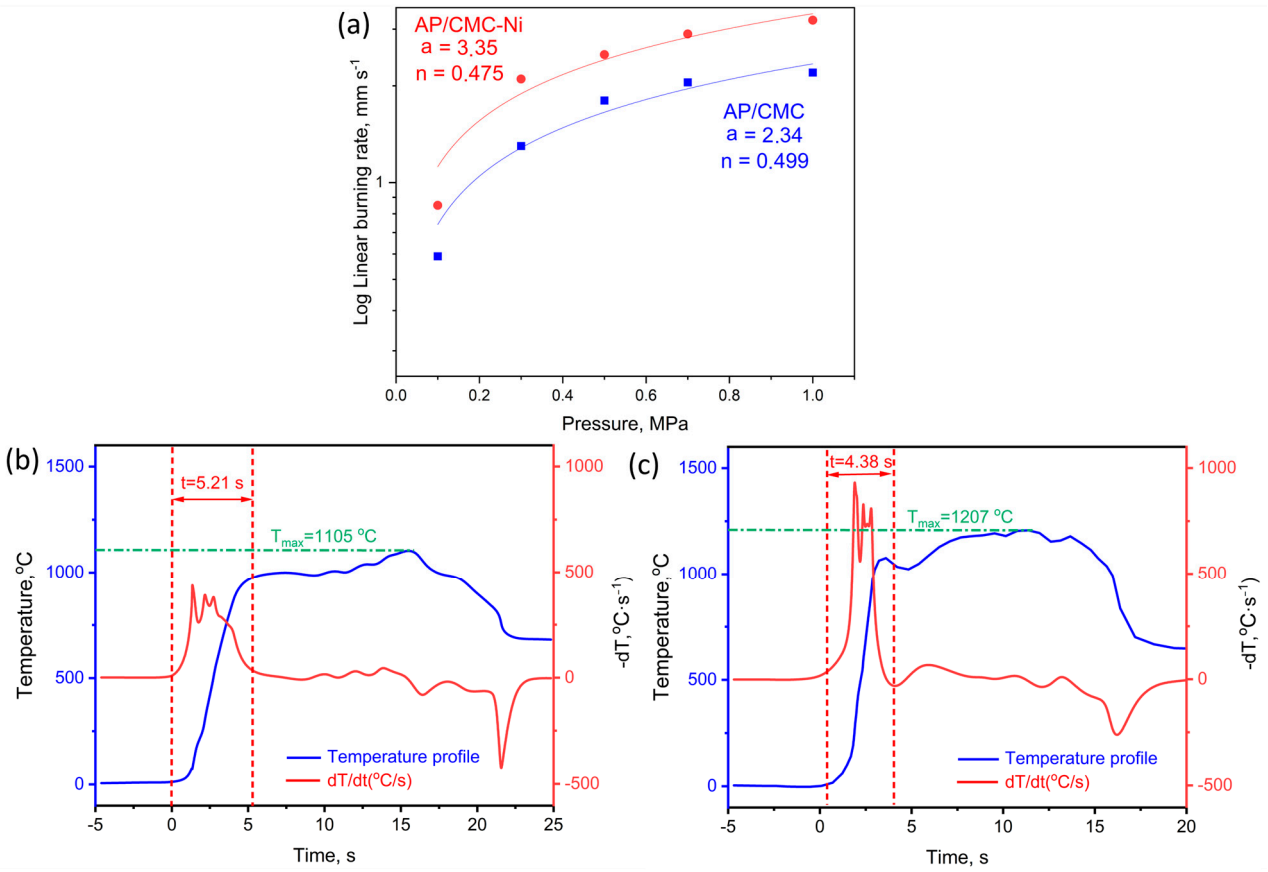

Figure 8. (**a**) Linear burning rates of AP/CMC and AP/CMC-Ni samples at different pressures. Thermal profiles of AP/CMC (**b**) and AP/CMC-Ni sample (**c**).

Figure 8c displays the thermal profile of the AP/CMC-Ni sample, where the T_{max} increases to 1207 °C, and the time to reach this temperature is reduced to 4.38 s. The steeper temperature rise in the blue curve and the more pronounced peaks in the rate of temperature change indicate a faster and more intense combustion process. The presence of nickel enhances thermal decomposition, likely acting as a catalyst that accelerates reaction kinetics and increases the heat release rate. The sharper peaks in dT/dt confirm a higher reaction rate, leading to a more rapid transition to peak combustion temperatures.

These results demonstrate that nickel incorporation significantly affects the combustion behavior of AP/CMC composites, leading to higher maximum temperatures and shorter combustion times, which are crucial factors for optimizing energetic material performance. The higher burning rates and the earlier rise to the maximum temperature in the AP/CMC-Ni samples suggest that nickel acts as a catalyst, improving the thermal degradation and combustion efficiency of the composite material. This improvement is beneficial for applications requiring rapid and efficient combustion processes.

In this study, we have demonstrated that Ni doping significantly enhances the combustion characteristics of AP/CMC composites, resulting in improved ignition stability and reduced decomposition temperature. It is important to note, however, that this formulation was not intended to meet the stringent energy requirements of high-performance rocket propellants. Additional modifications—such as incorporating more energetic binders or optimizing the oxidizer-to-fuel ratio—would be necessary to achieve the higher energy outputs demanded by advanced rocket propulsion. While our work focuses primarily on elucidating the role of Ni in these composites, future investigations may explore further enhancements in energy density, mechanical properties, and overall performance under conditions relevant to more demanding aerospace applications.

4. Conclusions

This study has demonstrated the significant impact of nickel doping on the thermal and combustion properties of ammonium perchlorate/carboxymethyl cellulose (AP/CMC) composites. The integration of nickel into the CMC matrix resulted in notable enhancements in the structural and functional characteristics of the composite material. The SEM-EDS analysis confirmed that nickel doping leads to thicker and more irregular CMC fibers, indicating substantial morphological changes. The FTIR spectroscopy revealed shifts in the O-H and C=O stretching bands, suggesting strong interactions between nickel ions and CMC functional groups. The XRD analysis showed a decrease in crystallinity and the presence of NiO phases, confirming the successful integration of nickel into the CMC matrix.

Thermal analyses, including DSC and TGA, showed that nickel doping significantly lowers the decomposition temperature of the AP/CMC composite and enhances the thermal degradation process. The AP/CMC-Ni composite exhibited a higher burning rate across all of the tested pressures, indicating the catalytic effect of nickel in improving the combustion efficiency. The constants derived from the power-law expression for burning rate further highlight the enhanced combustion performance due to nickel doping.

The findings highlight the crucial role of nickel doping in catalyzing the decomposition of ammonium perchlorate within the AP/CMC composite. By lowering the decomposition temperature, nickel enhances the overall combustion process, making the AP/CMC-Ni composite more efficient for applications requiring controlled thermal decomposition. These results provide valuable insights for the design and development of high-performance composite materials for advanced industrial applications.

Future research should focus on optimizing the level of nickel doping to maximize the material properties and exploring the effects of other metal dopants on the performance of CMC-based composites. Additionally, investigating the long-term stability and environmental impact of nickel-doped composites will be crucial for their practical application in various industries. It is also necessary to conduct a detailed investigation of the decomposition mechanism of the composite in the presence of the catalyst, including studies on activation energy and other kinetic parameters, to gain a deeper understanding of the catalytic processes involved.

Supplementary Materials: The following supporting information can be downloaded at: https://www.mdpi.com/article/10.3390/aerospace12040270/s1, Figure S1. Images of AP crystals. Figure S2. MicroXRF EDAX analysis for pure CMC sample. Figure S3. MicroXRF EDAX analysis for pure CMC-Ni sample. Figure S4. The FTIR spectra for 1M, 2M, 3M, and 4M Ni concentrations. Figure S5. XRD curve-fitting techniques using Gaussian functions.

Author Contributions: Conceptualization, M.N., M.J., M.O., M.A. and Z.B.; methodology, A.Y., M.M., M.Z., D.Y., A.L. and M.T.; validation, M.N., M.J., M.O., D.Y., M.T., A.L. and Z.B.; formal analysis, Z.B., M.M., M.A. and M.Z.; investigation, M.N., M.J., M.O., D.Y., A.L. and Z.B.; resources, A.Y. and M.M.; data curation, M.A. and M.Z.; writing—original draft preparation, Z.B. and M.A.; writing—review and editing, Z.B., M.A., A.L. and M.O.; visualization, Z.B. and M.A.; supervision, A.L. and Z.B.; project administration, A.L. and Z.B.; funding acquisition, M.N. All authors have read and agreed to the published version of the manuscript.

Funding: This work was funded by the Ministry of Science and Higher Education of the Republic of Kazakhstan, grant number BR249008/0224.

Data Availability Statement: Data are contained within the article.

Conflicts of Interest: The authors declare no conflicts of interest.

References

1. Mezroua, A.; Hamada, R.A.; Brahmine, K.S.; Abdelaziz, A.; Tarchoun, A.F.; Boukeciat, H.; Bekhouche, S.; Bessa, W.; Benhammada, A.; Trache, D. Unraveling the role of ammonium perchlorate on the thermal decomposition behavior and kinetics of NC/DEGDN energetic composite. *Thermochim. Acta* **2022**, *716*, 179305. [CrossRef]
2. Bekhouche, S.; Trache, D.; Abdelaziz, A.; Tarchoun, A.F.; Boukeciat, H. Effect of fluorine-containing thermite coated with potassium perchlorate on the thermal decomposition behavior and kinetics of ammonium perchlorate. *Thermochim. Acta* **2023**, *720*, 179413. [CrossRef]
3. Chen, T.; Hu, Y.W.; Zhang, C.; Gao, Z.J. Recent progress on transition metal oxides and carbon-supported transition metal oxides as catalysts for thermal decomposition of ammonium perchlorate. *Def. Technol.* **2021**, *17*, 1471–1485. [CrossRef]
4. Ma, D.; Li, X.; Wang, X.; Luo, Y. Research development on graphitic carbon nitride and enhanced catalytic activity on ammonium perchlorate. *RSC Adv.* **2021**, *11*, 5729–5740. [CrossRef] [PubMed]
5. Liang, T.; Yang, X.; Liu, B.; Song, R.; Xiao, F.; Yang, Y.; Wang, D.; Dong, M.; Ren, J.; Xu, B.B.; et al. Ammonium perchlorate@graphene oxide/Cu-MOF composites for efficiently catalyzing the thermal decomposition of ammonium perchlorate. *Adv. Compos. Hybrid Mater.* **2023**, *6*, 67. [CrossRef]
6. Zhang, J.; Jin, B.; Li, X.; Hao, W.; Huang, T.; Lei, B.; Guo, Z.; Shen, J.; Peng, R. Study of H2AzTO-based energetic metal-organic frameworks for catalyzing the thermal decomposition of ammonium perchlorate. *Chem. Eng. J.* **2021**, *404*, 126287. [CrossRef]
7. Deng, P.; Wang, H.; Yang, X.; Ren, H.; Jiao, Q. Thermal decomposition and combustion performance of high-energy ammonium perchlorate-based molecular perovskite. *J. Alloys Compd.* **2020**, *827*, 154257. [CrossRef]
8. Lei, G.; Zhong, Y.; Xu, Y.; Yang, F.; Bai, J.; Li, Z.; Zhang, J.; Zhang, T. New energetic complexes as catalysts for ammonium perchlorate thermal decomposition. *Chin. J. Chem.* **2021**, *39*, 1193–1198. [CrossRef]
9. Yaradoddi, J.S.; Banapurmath, N.R.; Ganachari, S.V.; Soudagar, M.E.M.; Mubarak, N.M.; Hallad, S.; Hugar, S.; Fayaz, H. Biodegradable carboxymethyl cellulose based material for sustainable packaging application. *Sci. Rep.* **2020**, *10*, 21960. [CrossRef]
10. Zhang, D.; Huang, Y. Dispersion characterizations and adhesion properties of epoxy composites reinforced by carboxymethyl cellulose surface treated carbon nanotubes. *Powder Technol.* **2022**, *404*, 117505. [CrossRef]
11. Li, X.; Cui, D.; Zhao, Y.; Qiu, R.; Cui, X.; Wang, K. Preparation of high-performance thermal insulation composite material from alkali-activated binders, foam, hollow glass microspheres, and aerogel. *Constr. Build. Mater.* **2022**, *346*, 128493. [CrossRef]
12. Luna-Martínez, J.F.; Reyes-Melo, E.; González-González, V.; Guerrero-Salazar, C.; Torres-Castro, A.; Sepúlveda-Guzmán, S. Synthesis and characterization of a magnetic hybrid material consisting of iron oxide in a carboxymethyl cellulose matrix. *J. Appl. Polym. Sci.* **2013**, *127*, 2325–2331. [CrossRef]
13. Gan, T.; Zhang, Y.; Su, Y.; Hu, H.; Huang, A.; Huang, Z.; Chen, D.; Yang, M.; Wu, J. Esterification of bagasse cellulose with metal salts as efficient catalyst in mechanical activation-assisted solid phase reaction system. *Cellulose* **2017**, *24*, 5371–5387. [CrossRef]
14. El-Lateef, H.M.A.; Albokheet, W.A.; Gouda, M. Carboxymethyl cellulose/metal (Fe, Cu, and Ni) nanocomposites as non-precious inhibitors of C-Steel corrosion in HCl solutions: Synthesis, Characterization, Electrochemical and Surface Morphology Studies. *Cellulose* **2020**, *27*, 8039–8057. [CrossRef]
15. Kamel, S.; Khattab, T.A. Recent advances in cellulose supported metal nanoparticles as green and sustainable catalysis for organic synthesis. *Cellulose* **2021**, *28*, 4545–4574. [CrossRef]
16. Pinto, E.; Aggrey, W.N.; Boakye, P.; Amenuvor, G.; Sokama-Neuyam, Y.A.; Fokuo, M.K.; Karimaie, H.; Sarkodie, K.; Adenutsi, C.D.; Erzuah, S.; et al. Cellulose processing from biomass and its derivatization into carboxymethylcellulose: A Review. *Sci. Afr.* **2022**, *15*, e01078. [CrossRef]
17. Nasrollahzadeh, M.; Shafiei, N.; Nezafat, Z.; Bidgoli, N.S.S.; Soleimani, F. Recent progresses in the application of cellulose, starch, alginate, gum, pectin, chitin, and chitosan-based (nano) catalysts in sustainable and selective oxidation reactions: A review. *Carbohydr. Polym.* **2020**, *241*, 116353. [CrossRef]
18. Harimech, Z.; Toshtay, K.; Atamanov, M.; Azat, S.; Amrousse, R. Thermal decomposition of ammonium dinitramide (ADN) as green energy source for space propulsion. *Aerospace* **2023**, *10*, 832. [CrossRef]
19. Atamanov, M.; Yelemessova, Z.; Imangazy, A.; Kamunur, K.; Lesbayev, B.; Mansurov, Z.; Yan, Q.L. The catalytic effect of CuO-doped activated carbon on thermal decomposition and combustion of AN/Mg/NC composite. *J. Phys. Chem. C* **2019**, *123*, 22941–22948. [CrossRef]
20. Zhou, X.; Xu, R.; Nie, H.; Yan, Q.; Liu, J.; Sun, Y. Insight into the precise catalytic mechanism of CuO on the decomposition and combustion of core–shell Al@AP particles. *Fuel* **2023**, *346*, 128294. [CrossRef]
21. Yadav, N.; Srivastava, P.K.; Varma, M. Recent advances in catalytic combustion of AP-based composite solid propellants. *Def. Technol.* **2021**, *17*, 1013–1031.
22. Zhang, T.; Shi, H.; Zhang, Y.; Liu, Q.; Fei, W.; Wang, T. Hollow flower-like nickel particles as the promoter of ammonium perchlorate-based solid propellant. *Appl. Surf. Sci.* **2021**, *552*, 149506. [CrossRef]
23. Xu, Y.; Wang, Y.; Zhong, Y.; Lei, G.; Li, Z.; Zhang, J.; Zhang, T. Transition metal complexes based on hypergolic anions for catalysis of ammonium perchlorate thermal decomposition. *Energy Fuels* **2020**, *34*, 14667–14675. [CrossRef]

24. Liang, T.; Song, R.; Chen, C.; Alomar, T.S.; Xiao, F.; AlMasoud, N.; El-Bahy, Z.M.; Yang, Y.; Algadi, H.; Sun, L. Graphene oxide–supported Cu/Co nano-catalysts for thermal decomposition of ammonium perchlorate composites. *Adv. Compos. Hybrid Mater.* **2023**, *6*, 188.
25. Zhang, J.; Jin, B.; Peng, R. Construction of cobalt–nickel bimetallic coordination polymers and their catalytic thermal decomposition of ammonium perchlorate. *Appl. Surf. Sci.* **2024**, *647*, 158970.
26. Fang, H.; Xu, R.; Yang, L.; Mi, Z.; He, Q.; Shi, H.; Jiang, L.; Fu, X.; Zhang, G. Facile fabrication of carbon nanotubes-encapsulated cobalt (nickel) salt nanocomposites and their highly efficient catalysis in the thermal degradation of ammonium perchlorate and hexogen. *J. Alloys Compd.* **2022**, *928*, 167134.
27. Hu, Y.; Wang, X.; Hao, J.; Jiang, S.; Zhang, J.; Yang, Y.; Lin, K.; Zheng, J.; Shuai, Y. The catalytic thermal decomposition of ammonium perchlorate on CuMxOy (M = Fe, Ni, Co, and Zn) catalysts and their applications in solid propellant. *J. Therm. Anal. Calorim.* **2023**, *148*, 6013–6026.
28. Chen, J.; Huang, B.; Liu, Y.; Qiao, Z.; Li, X.; Lv, G.; Yang, G. 3D hierarchically ordered porous carbon entrapped ni nanoparticles as a highly active catalyst for the thermal decomposition of ammonium perchlorate. *Energ. Mater. Front.* **2021**, *2*, 14–21.
29. Chandrababu, P.; Beena, S.; Thomas, D.; Thankarajan, J.; Sukumaran Nair, V.; Raghavan, R. TG-MS study on the activity of Fe, Co, Ni, Cu, and Zn nanometal catalysts on thermal decomposition of ammonium perchlorate. *J. Therm. Anal. Calorim.* **2023**, *148*, 10065–10079.
30. Liu, Y.H.; Zheng, J.; Yu, G.B.; Qia, J.; Xu, Q.Q.; Zhang, C.M.; Zhang, X. Graphene-based composites for the thermal decomposition of energetic materials. *Mater. Sci. Forum* **2021**, *1027*, 123–129.
31. Shmakov, A.G.; Paletsky, A.A.; Netskina, O.V.; Dmitruk, K.A.; Komova, O.V.; Mukha, S.A. Kinetics and composition of gaseous products of pyrolysis of organometallic complexes of nickel, iron, and copper with inorganic anions. *Combust. Explos. Shock Waves* **2024**, *60*, 25–41. [CrossRef]
32. Akhinzhanova, A.; Sultahan, S.; Tauanov, Z.; Mansurov, Z.; Capobianchi, A.; Amrousse, R.; Atamanov, M.; Yan, Q.-L. Preparation and evaluation of effective thermal decomposition of tetraamminecopper (ii) nitrate carried by graphene oxide. *Combust. Flame* **2023**, *250*, 112672. [CrossRef]
33. Barakat, A.; Kamoun, E.A.; El-Moslamy, S.H.; Ghazy, M.B.; Fahmy, A. Photo-curable carboxymethylcellulose composite hydrogel as a promising biomaterial for biomedical applications. *Int. J. Biol. Macromol.* **2022**, *207*, 1011–1021. [CrossRef]
34. Meiirbekov, M.N.; Ismailov, M.B.; Kenzhegulov, A.K.; Mustafa, L.M.; Tashmukhanbetova, I.B. Study of the effect of combined reinforcement and modification of epoxy resin with rubbers on the impact strength of carbon fiber-reinforced plastic. *Eurasian J. Phys. Funct. Mater.* **2024**, *8*, 23–32. [CrossRef]
35. Tangthuam, P.; Pimoei, J.; Mohamad, A.A.; Mahlendorf, F.; Somwangthanaroj, A.; Kheawhom, S. Carboxymethyl cellulose-based polyelectrolyte as cationic exchange membrane for zinc-iodine batteries. *Heliyon* **2020**, *6*, e01078. [CrossRef] [PubMed]
36. Olanipekun, E.O.; Ayodele, O.; Olatunde, O.C.; Olusegun, S.J. Comparative studies of chitosan and carboxymethyl chitosan doped with nickel and copper: Characterization and antibacterial potential. *Int. J. Biol. Macromol.* **2021**, *183*, 1971–1977. [CrossRef] [PubMed]
37. Wang, X.; Du, Y.; Fan, L.; Liu, H.; Hu, Y. Chitosan-metal complexes as antimicrobial agents: Synthesis, characterization, and structure-activity study. *Polym. Bull.* **2005**, *55*, 105–113. [CrossRef]
38. Mohammadkhani, A.; Mohammadkhani, F.; Farhadyar, N.; Sadjadi, M.S. Novel nanocomposite zinc phosphate/polyvinyl alcohol/carboxymethyl cellulose: Synthesis, characterization, and investigation of antibacterial and anticorrosive properties. *Case Stud. Chem. Environ. Eng.* **2024**, *9*, 100591. [CrossRef]
39. Taurbekov, A.; Kaidar, B.; Baltabay, A.; Imash, A.; Ko, W.-B.; Ko, J.-W.; Atamanov, M.; Mansurov, Z.; Smagulova, G. Valorization of Grass Clipping Waste: A Sustainable Approach to Cellulose Extraction and Paper Manufacturing. *Appl. Sci.* **2024**, *14*, 6680. [CrossRef]
40. Yao, W.; Weng, Y.; Catchmark, J.M. Improved Cellulose X-Ray Diffraction Analysis Using Fourier Series Modeling. *Cellulose* **2020**, *27*, 5563–5579. [CrossRef]
41. Zhang, J.; Wang, Y.; Zhang, L.; Zhang, R.; Liu, G.; Cheng, G. Understanding Changes in Cellulose Crystalline Structure of Lignocellulosic Biomass during Ionic Liquid Pretreatment by XRD. *Bioresour. Technol.* **2014**, *151*, 402–405. [CrossRef] [PubMed]
42. Zhao, Z.; Zhang, C.; Mu, X.; Li, M.; Ren, Y.; Li, J.; Zhao, F.; Ma, H. Decomposition Reaction Mechanism of Ammonium Perchlorate on N-Doped Graphene Surfaces: A Density Functional Theory Study. *Molecules* **2025**, *30*, 837. [CrossRef] [PubMed]
43. Li, J.; Liu, X.; Xie, Q.; Su, J.; Hu, M.; Yao, Z. Effect of Perchlorate on Combustion Properties of Directly-Written Al/PVDF Composites. *Fire* **2023**, *6*, 106. [CrossRef]

Disclaimer/Publisher's Note: The statements, opinions and data contained in all publications are solely those of the individual author(s) and contributor(s) and not of MDPI and/or the editor(s). MDPI and/or the editor(s) disclaim responsibility for any injury to people or property resulting from any ideas, methods, instructions or products referred to in the content.